Towards simulating flow induced spillage in dredge cutter heads using DEM-FVM

Nieuwboer, B.J.; van Rhee, C.; Keetels, G.H.

DOI
10.1016/j.oceaneng.2023.113922

Publication date
2023

Document Version
Final published version

Published in
Ocean Engineering

Ocean Engineering 275 (2023) 113922

Contents lists available at ScienceDirect

Ocean Engineering

journal homepage: www.elsevier.com/locate/oceaneng

Towards simulating flow induced spillage in dredge cutter heads using DEM-FVM☆

B.J. Nieuwboer [a,*], C. van Rhee [b], G.H. Keetels [b]

[a] Royal IHC, Smitweg 6, Kinderdijk, 2961 AW, The Netherlands
[b] Delft University of Technology, Mekelweg 5, Delft, 2628 CD Delft, The Netherlands

ARTICLE INFO

Keywords:
Dredging
Cutter Suction Dredger
Computational fluid dynamics
Dynamic mesh
Discrete Element Method
OpenFOAM

ABSTRACT

When dredging rock using a Cutter Suction Dredger the high amount of spillage is problematic, since it prevents an energy efficient removal process. This papers presents a coupled DEM-FVM method to simulate spillage, that can be used for optimizing the design and working method of the Cutter Suction Dredger. In these simulations, the challenge was to model relatively large particles in a complex and rotating geometry. To ensure stability and reduce computational time we used smoothing kernels to map the forces and the concentration between the discrete elements and the fluid mesh. The method is validated for the fluid flow in the rotating cutter head. This model incorporates all physical processes to predict flow induced spillage in cutter heads within feasible calculation times.

1. Introduction

1.1. A cutter suction dredger

Dredging equipment is specialized in the removal of soil from the sea- or river bed in order to create or maintain a navigable depth. A Cutter Suction Dredger is one of such dredge vessels (Fig. 1). It can be employed for dredging all kinds of soils: sand, clay and softer rock like sandstone or limestone.

The Cutter Suction Dredger has a cutter head with pickpoints attached to it (Fig. 2). Its cutter head rotates, swings and pushes its pickpoints into the seabed and thereby disintegrating the soil. Due to the shape of the blades, the soil is picked up and transported towards the suction tube. Here, the soil–water-mixture is hydraulically transported to the vessel, from where it is transported again to a discharge location. In the cutter head, the suction flow together with the rotating motion of the blades keep the particles in suspension before these are sucked up.

For sandy soils, the removal process is much more efficient compared to rock. Sand is easily kept in suspension before it is sucked up. Sandstone and limestone do not totally disintegrate when the pickpoints cut through the soil. The large pieces of rock are more influenced by gravity and the centrifugal force and are therefore thrown out of the cutter head more easily than smaller sand particles. The problem with these pieces leaving the cutter head is that they will stay on the seabed, which is called spillage.

Fig. 1. Cutter Suction Dredger 'Athena' owned by van Oord.

A Cutter Suction Dredger has two options to create a certain delivered depth when much material is spilled. Either the dredger has to pass over the area another time or they have to remove a larger amount of material than needed for the desired depth and leave the spilled material on the bed. This second method is called dredging an

☆ This research is funded by Royal Boskalis Westminster and Van Oord Dredging and Marine Contractors.
* Corresponding author.
E-mail addresses: b.nieuwboer@royalihc.com (B.J. Nieuwboer), C.vanRhee@TUDelft.nl (C. van Rhee), G.H.Keetels@TUDelft.nl (G.H. Keetels).

https://doi.org/10.1016/j.oceaneng.2023.113922
Received 29 September 2022; Received in revised form 7 January 2023; Accepted 7 February 2023
Available online 15 March 2023

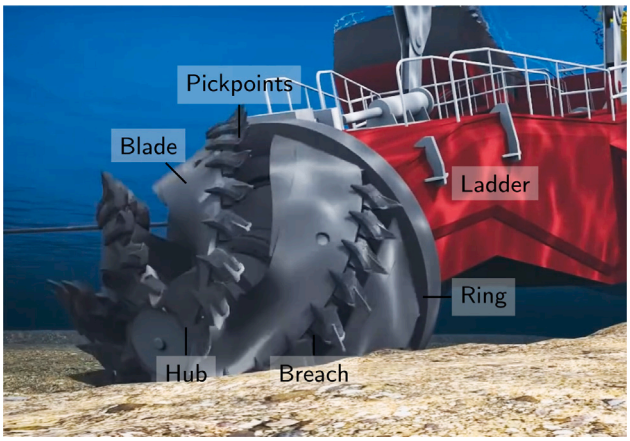

Fig. 2. A cutter head; the important parts are labelled (Royal Boskalis Westminster N.V., 2016).

over-depth. Both options are less energy efficient and take more time to complete than dredging the delivered depth with limited spillage.

In general two types of spillage can be defined: spillage due to cutting and spillage due to mixing. Spillage due to cutting includes the soil that is cut, but never enters the cutter head. The soil which, after entering the cutter head, is thrown out again, is defined as being spilled due to mixing. This paper will focus on the spillage due to mixing when cutting rock. It will in particular focus on the flow induced spillage of rock in cutter heads, which is a sub-type of the spillage due to mixing. It is the spillage caused by outflow underneath the ring.

When the processes causing the spillage are accurately described, the design of the cutter head and the working method can be adapted to reduce the amount of spillage, leading to a more energy efficient dredging operation.

This paper presents the technical feasibility of a novel numerical method for simulating flow induced spillage of pieces of rock in cutter heads. It will show validated results of the fluid flow in a cutter head, particle–fluid interaction, particle–particle and particle–blade interactions.

This method can be used for the optimizing of the design of the Cutter Suction Dredger and for optimizing the working method. New designs of cutter head geometries and working methods can be assessed prior to experimental testing on lab and prototype scale, which are both expensive to perform. Secondly, a numerical model delivers more detailed information on the fluid velocities and of the pieces of rock, which can be helpful to find ways to improve the cutter head design. In this paper, the method will be validated for the fluid flow in the cutter head. The trend flow induced spillage will be compared to existing measurements.

1.2. Literature review

Slotta (1968) used hydrogen bubbles for investigating the flow around a cutter head with a ring diameter of 0.165 m to improve the hydrodynamic efficiency using different geometries.

Dekker et al. (2003) measured the velocities in and around a schematized cutter head including a backplate and suction tube using an Acoustic Doppler Velocimeter (ADV). The ADV measures the velocity at a distance of approximately 5 cm from the probe. This distance from the probe minimizes the disturbance of the flow measurement. Measurements are taken at 12 positions in the cutter head using a single ADV; for each measurement location the ADV was relocated. Steinbusch et al. (1999) and Dekker et al. (2003) created a potential flow model of this schematized cutter head. The model predicted the steady potential flow. By simulating different blade positions it was possible to use Fourier analysis to construct a time signal. This constructed time-series was time-averaged. It compared reasonably well with measured data.

Zhang et al. (2016) modelled the velocities in a full scale (2.8 m) cutter head without a backplate or pickpoints using the Reynolds Averaged Navier–Stokes Equations in Ansys Fluent. The model used a Multiple Reference Frame (MRF) approach for simulating the rotating blades in a steady simulation. In this approach the blades do not rotate in the domain, but the fictitious forces are added to the Navier–Stokes Equations.

Den Burger (2003) and Den Burger et al. (1999) performed experiments in cutting of blocks of cemented gravel using a ring diameter of 0.4 m for a 1 to 8 scale cutter head. The gravel used in this experiment had a median diameter of 0.01 m and a density of 2650 kg/m^3. For each suction velocity the experiments showed an optimal rotational speed of the cutter, where the production fraction is maximum. Den Burger (2003) explained this using two regimes. At a high rotational speed, both the centrifugal force on the particles and the outward flow near the ring increases, due to the shape of the cutter head. Both effects lead to an outward movement of the particles, leading to more spillage near the ring. In the second regime, occurring at low rotational speed, the production fraction increases with increasing rotational speed. Den Burger (2003) hypothesized a better mixing of the particles due to collisions with the faster moving blades at higher rotational speeds caused this effect. This leads to more particles in suspension, which enter the suction mouth easier and are therefore less likely spilled.

Den Burger (2003) created three Discrete Element Models for studying the particle behaviour in a rotating cutter head: a model of particles in a vortex flow with a sink describing the suction mouth using a potential flow model (Den Burger, 1997). A second model described the motion of a particle in contact with a rotating blade in the same vortex flow (Den Burger, 2001). The third model combined the potential flow computations of Dekker et al. (2003) for the blades and suction mouth with the transport model of a particle along a rotating blade (Den Burger et al., 2002).

For simulating spillage and production, Zhang et al. (2018) extended the fluid model of Zhang et al. (2016) with pickpoints, a backplate and a suction tube. They used the Discrete Element Model to model the particles in the cutter head and used an unsteady Reynolds Averaged Navier-Stokes (URANS) approach for modelling the fluid. The particles were injected from the blades and had a particle diameter of 1 to 5 mm. The rotating cutter head was modelled using a Multiple Reference Frame, indicating that the blades did not rotate in the model. This means that the blades could not transport the particles towards the suction mouth as was observed and modelled by Den Burger (2003). Secondly, only the collisions between the particles and the cutter head are taken into account and not the inter-particle collisions. Because of this no bed of particles can form in the cutter, which was observed by Den Burger (2003) during his experiments. The results showed an increase in production with increasing suction discharge and a decreasing production with increasing rotational velocity. The used suction velocities were low compared to values used in practice and low compared to the velocities used by Den Burger (2003). This might explain the low production fraction they obtained compared to the gravel cutting experiments of Den Burger (2003).

Werkhoven et al. (2018, 2019) and Miedema (2019) derived an analytical model for determining the spillage in a rotating cutter head. They based the model on the affinity laws for centrifugal pumps for both the pressure and the discharge. These models are calibrated on the available measured spillage data, but are not based on elementary physical processes.

None of the mentioned models is suitable for accurately modelling flow induced spillage, since they all lack some physical processes. Of the 3 models of Den Burger (2003), the potential flow model was the most complete. It discarded the inter-particle collisions and the

concentration effect. The model of Zhang et al. (2018) disregarded the physical motion of the rotating blades and the concentration effect on the drag of the particles. From the description in the paper it is not clear if the particles influence the density in the momentum equation of the fluid/mixture and if the resulting forces of the Discrete Element Model act on the fluid. Secondly, the simulated particle sizes of 1 to 5 mm are very small compared to a typical size of the cut material, which measures in the order of 100 mm.

1.3. Modelling

To analyse flow induced spillage in a cutter head, the mechanisms causing this spillage should be included in the model. This could be modelled using a drift-flux approach (Ishii and Hibiki, 2011; Manninen et al., 1996), an Euler–Euler approach (Ishii and Hibiki, 2011), or an Euler–Lagrange approach (Zhou et al., 2010). In this paper, the spillage is modelled using an Euler–Lagrange model, which is better suitable to model spillage than an Euler–Euler or Drift-Flux model for the reasons described further on.

Both continuum models only output the Eulerian velocity and concentration and not a particle trajectory. Since these are needed to accurately visualize the mechanisms causing spillage, both the Euler–Euler method and the Drift-Flux model are less suitable. An Euler–Euler model needs a collision model for a volume of particles; for example, the kinetic theory. However, this is designed for near equilibrium conditions, which are not present in the rotating cutter head. It is unknown if the collisional and particle contact forces at the blades and in the near-blade region can be approximated with kinetic theory or rheological formulations. This is a disadvantages for both Euler–Euler and Drift-flux. In an Euler–Lagrange model the collisions are resolved.

Both the Drift-Flux model and the Euler–Euler model, need a special boundary condition for the slip velocity of the particles at the wall, while in the Euler–Lagrange model this follows from the validated collision model.

A Drift-Flux model has the underlying assumption that the forces on the dispersed phase are in equilibrium. The dispersed phase does therefore not accelerate with respect to the mixture, while the mixture as a whole can accelerate. Large pieces of rock take a relatively long time to accelerate to this terminal settling velocity (high Stokes number), therefore this assumption does not hold. It is possible to model the full transient equation for relative velocity of the dispersed phase (Manninen et al., 1996). However, the forces will not act back on the momentum equation of the fluid/mixture.

Four-way coupling is essential for modelling the particle trajectories since Den Burger (2003) observed high concentrations at the blades in his experiments. In four-way coupling the fluid forces act on the particles, resulting forces act on the fluid and collisions are modelled.

In the simulations Den Burger (2001), observed the transport of particles towards the suction mouth by the rotating blades. To model this transport mechanism, the model should include rotating blades.

The model should therefore capture the following three phenomena: flow induced by the rotating blades of a cutter head, particle–flow interaction and collisions between the particles and of the particles with the blades. OpenFOAM v1712 is able to model most of these phenomena. Therefore, this software will be used as a basis for the model and since OpenFOAM is open-source the code can be adapted and extended to include the missing models, which will elaborated on in the next section.

2. Computational method

The method for modelling the flow induced spillage consists of four parts: modelling the fluid phase using the Finite Volume Method (FVM), modelling the particle trajectories using the Discrete Element Method (DEM), coupling between DEM and the fluid, and lastly the collisions between the particles and the particles with the cutter head. Each of these four methods will be described in this section.

In the simulation, a minimal mesh cell resolution is needed to represent blade geometry accurately and to solve velocity gradients near the blade surface. A typical particle size of the cut material is 100 mm on prototype scale, which is an order larger than the mesh size near the wall. On the 1 to 4 model scale used in this paper, a particle is typically 2 to 5 times larger than the mesh cells. This results in a conflict of scales: for solving the fluid flow features a fine mesh is needed, while the mesh should be coarser than the particles to be able to use standard DEM-FVM coupling, which assumes small particles in a large mesh cell. Typically, an immersed boundary method (IBM) would be suitable when particles are larger than the fluid cells. However, this is too expensive since it requires an even finer mesh for well-reproducing the drag force on a particle. Bigot et al. (2014) showed an error of nearly 50% in computing the drag coefficient on a settling particle for a sphere 5 times as big as a cell.

In this paper we will use the coupling of the DEM with the FVM as presented by Xiao and Sun (2011) to simulate the flow induced spillage and study the physical realism of the results. This method is verified against a numerical integration of the equation of motion to ensure a well-predicted settling velocity.

In implementing this method into OpenFOAM, special care was taken for mapping particles near walls and interfaces, such as the sliding mesh interface and the processor interface.

2.1. Flow model: Navier–Stokes

Zhou et al. (2010) and Hofman (2015) describe the Navier–Stokes Equations with variable fluid fraction and the coupling with DEM. The momentum equation, continuity equation and the phase fraction continuity for the fluid phase coupled with DEM are, respectively:

$$\frac{\partial \alpha_c \boldsymbol{u_c}}{\partial t} + \nabla \cdot \left(\alpha_c \boldsymbol{u_c}\, \boldsymbol{u_c}\right) = -\frac{1}{\rho_c}\nabla p + \nabla \cdot \left(\alpha_c \bar{\bar{\tau}}\right) + \boldsymbol{g} + \frac{\boldsymbol{f_i}}{\rho_c} \tag{1}$$

$$\frac{\partial \alpha_c}{\partial t} + \nabla \cdot \left(\alpha_c \boldsymbol{u_c}\right) = 0 \tag{2}$$

$$\alpha_c + \alpha_p = 1 \tag{3}$$

where α_c is the continuous phase (or fluid phase) fraction [–], α_p is the particle phase fraction [–], ρ_c is the continuous phase (or fluid phase) density [kg/m^3], $\boldsymbol{u_c}$ is the continuous phase (or fluid phase) velocity [m/s], t is the time [s], $\bar{\bar{\tau}}$ is the effective stress tensor including both the viscous and turbulent shear stresses acting on the fluid [N/m^2], p is the pressure acting on the continuous phase [N/m^2], $\boldsymbol{f_i}$ is the interaction force of the discrete particles acting on the fluid per unit volume [N/m^3], $\boldsymbol{g}$ is the gravitational acceleration [m/s^2].

For modelling the turbulent shear stresses the Realizable k-ϵ Turbulence model of Shih et al. (1995) is used. The momentum and continuity equation are discretized using the method described by Jasak (1996) for single phase flow. It is solved by using the PIMPLE method, which is a combination of the PISO and SIMPLE method (Weller, 2005). This is based on the standard PISO algorithm described in Versteeg and Malalasekera (2007). In these methods the momentum and continuity equation are solved by constructing the pressure Poisson equation. Solving this equation leads to the pressure at the new time step, which in turn is used to compute the velocities at the new time step. The time derivative of the concentration in the continuity equation (first term in Eq. (2)) enters the right hand side of the pressure Poisson equation. When this term becomes large, solving the pressure Poisson equation takes more iterations/time and can lead to unstable simulation results.

Sliding mesh

OpenFOAM solves the interface of the rotating motion between two parts of the mesh using a sliding mesh interface based upon the method of Farrell and Maddison (2011). It couples the rotating part of a mesh with the stationary part using area mapping: the values on target faces are computed based on the overlapping face area of the source faces.

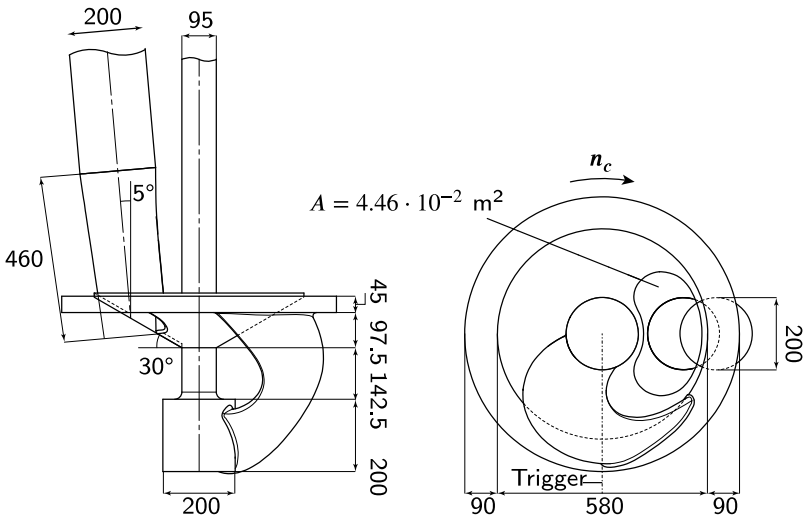

Fig. 3. Front and bottom view of the cutter head used in the experiments by Dekker et al. (2003) and the simulations of these experiments presented in this paper. For clarity only one of the blades of the cutter head is visualized, while in reality the cutter head has 6 blades. The measurements are in mm and the area A in m^2.

Validation

For single phase flow the sliding mesh interface is validated using the circular Couette flow for which an analytical solution exists. The velocities in the rotating cutter head are validated against the experiments of Dekker et al. (2003) and yet unpublished data obtained during that measurement campaign (Section 3.1).

2.2. Particle model: Discrete element method

The motion of particles is described using Newton's second law. The forces acting on the particle are described by Maxey and Riley (1983) or Zhou et al. (2010), leading to:

$$V_p \rho_p \frac{\partial \boldsymbol{u}_p}{\partial t} = \frac{1}{2} C_d A_p \rho_c \left(\boldsymbol{u}_{c|p} - \boldsymbol{u}_p\right) \left\|\boldsymbol{u}_{c|p} - \boldsymbol{u}_p\right\| \alpha_c^{-\beta+1} + C_{AM} V_p \rho_c \left(\frac{D\boldsymbol{u}_{c|p}}{Dt} - \frac{\partial \boldsymbol{u}_p}{\partial t}\right) + V_p \frac{D\boldsymbol{u}_{c|p}}{Dt} + V_p \left(\rho_p - \rho_c\right) \boldsymbol{g} \tag{4}$$

where V_p is the volume of the particle [m^3], ρ_p is the density of the particle [kg/m^3], $\boldsymbol{u_p}$ is the particle velocity [m/s], C_d is the drag coefficient [–], A_p is the area of the particle projected to the flow direction [m^2], $\boldsymbol{u_{c|p}}$ is the undisturbed fluid velocity at the particle location [m/s], C_{AM} is the added mass coefficient, typically taken as 0.5 [–], $\boldsymbol{g}$ is the gravitational acceleration [m/s^2], β is the hindered settling exponent for the drag force [–].

The term on the left-hand side of Eq. (4) is the inertia, the terms on the right-hand side denote the drag force (corrected for the concentration effect), the added mass force, the pressure gradient force and the combined effect of gravity and buoyancy. For including this equation in OpenFOAM, the specific drag formulation and the hindered settling exponent had to be included. The drag coefficient is computed using the formulation of (Brown and Lawler, 2003):

$$C_d = \frac{24}{\mathrm{Re_s}} \left(1 + 0.150\ \mathrm{Re_s}^{0.681}\right) + \frac{0.407}{1 + 8710\ \mathrm{Re_s}^{-1}} \quad \text{for} \quad \mathrm{Re_s} \leq 2 \cdot 10^5 \tag{5}$$

$$\mathrm{Re_s} = \frac{\left\|\boldsymbol{u}_{c|p} - \boldsymbol{u}_p\right\| d_p}{\nu} \tag{6}$$

where $\mathrm{Re_s}$ is the Reynolds number defined by the slip velocity between the particles and the fluid [–], d_p is the particle diameter [m], and ν is the kinematic viscosity of the fluid fraction [m^2/s^2].

To account for the concentration effect the influence of increased concentration on the drag of a particle ($\boldsymbol{F_d}$) is used (Di Felice, 1994):

$$\boldsymbol{F_d} = \boldsymbol{F_{d,0}}\ \alpha_c^{-\beta+1} \tag{7}$$

where $\boldsymbol{F_d}$ is the drag force on a particle influenced by the concentration due to the presence of neighbouring particles [N], $\boldsymbol{F_{d,0}}$ is the drag force on a single particle in absence of surrounding particles [N]

Richardson and Zaki (1954) derived that the exponent β in this equation has a negative value, which increases the drag on a particle with an decreasing void fraction (or continuous phase fraction) In this case the expression of Di Felice (1994) is used:

$$\beta = 3.7 - 0.65\ \exp\left(-\frac{1}{2}\left(1.5 - \log_{10} \mathrm{Re_p}\right)^2\right) \tag{8}$$

where $\mathrm{Re_p}$ is defined as:

$$\mathrm{Re_p} = \frac{\alpha_c \left\|\boldsymbol{u}_{c|p} - \boldsymbol{u}_p\right\| d_p}{\nu} \tag{9}$$

2.3. Coupling DEM and fluid

Coupling the DEM with the FVM is challenging, since the underlying assumption of the DEM is a small particle to cell ratio. Mapping particles larger than a cell lead to two problems. The first is the particle concentration exceeding one, which is not physical. Secondly, the forces computed in the DEM are based on undisturbed fluid velocity. When coupling particles with the fluid, the local fluid velocity is disturbed by the presence of the particle. For a few small particles in large computational fluid cell this is no issue. For larger particles, e.g. a large particle in a cell of about the same size as the particle, this forms a problem. A representative fluid velocity needs to be determined for the drag computations.

For computing this representative fluid velocity, this paper describes a kernel function for mapping the fluid velocities to particles. Sun and Xiao (2015b) compared five different coupling methods for large particles:

1. Particle centroid method. This method uses the fluid velocity from the finite volume cell to compute the drag force. The concentration in the cell where the particle centre is located, is computed by dividing the particle volume by the cell volume.
2. Divided particle method. This method also uses the fluid velocity from the finite volume cell. The difference between this method and the previous is the computation of the concentration occurs for each cell the particle intersects with. Computing the amount of volume of a particle located in each cell is a complex procedure for irregular shaped cells, making this approach not suitable for this application. Secondly, this approach only works

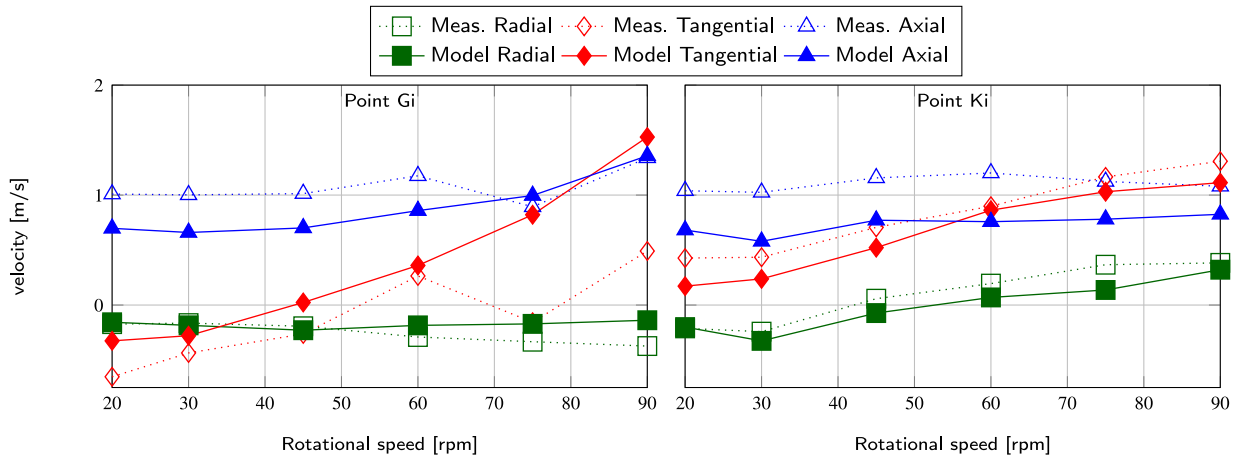

Fig. 4. Velocity components against the rotational velocity for two points. The locations of these points are shown in Fig. 6. The measured velocities are denoted with dotted lines. The modelled velocities have solid lines.

for particles which are smaller than the mesh cells, while the particles in the cutter head are a factor 2 to 5 larger than the mesh cells.

3. Two-grid approach. Another way of mapping the particles is making use of a second coarser mesh. In this two-grid approach the particles interact with this coarser mesh. The concentration, fluid velocities and the particle forcing are mapped between the coarse and the fine mesh. This results in a smooth distribution of the concentration. However, implementing this method is complex for irregular cells combined with a sliding mesh and multiple processor cores.
4. Statistical kernel. Xiao and Sun (2011) used a statistical kernel function to map the data between the Lagrangian and Eulerian phase. All the cells in a specified influence sphere around the particle are used for mapping the Eulerian and Lagrangian data. Cells closer the particle centre have a bigger influence than the cells at a larger distance from the centre.
5. Diffusion method. Sun and Xiao (2015b) updated the kernel method of Xiao and Sun (2011) to a method where not every single particle would be smoothed. An initial concentration and force field is smoothed. First, the particle forcing and concentration are mapped to the cell containing the centre of the particle. This step is the same as in the particle centroid method. Afterwards, a diffusion equation is applied to the particle concentration and forcing fields. This leads to smoothed field variables. The method is also applied to the fluid velocity field acting on the particles for estimating the undisturbed fluid velocity at the centre of the particle.

Of these five described coupling methods the particle centroid method and divided particle method are not suitable for particles much larger than a cell size. The two-grid method is not suitable, since two similar boundary fitted meshes are needed, which is not practical for a complicated geometry such as a rotating cutter head. This leaves the statistical kernel method and the diffusion method. The kernel method allows for a smooth transition of the concentration field in time, which is needed to compute a continuous return flow around the particle when using the continuity equation in the form of Eq. (2). Sun and Xiao (2015b,a) use the diffusion method in combination with a different continuity equation, which is likely more capable to handle a discontinuous time derivative of the concentration field.

The novelty of this paper is extending the methods of Xiao and Sun (2011) and Sun and Xiao (2015b,a) for simulating large particles in rotating machinery. For this purpose the interaction of the kernel function with a sliding mesh interface is incorporated.

The remainder of this section shows the mapping of the particle velocities, volumes and forces to the fluid and the mapping of the fluid velocity, fluid acceleration and fluid phase fraction to the particles. Thereafter, it shows treatment of the boundaries when using this mapping.

Particle to fluid

For the kernel method the particle fraction at a cell is computed by the volume of the particle multiplied by a Gaussian kernel ($\phi(r_{j,n})$) ensuring a higher particle fraction near the centre of the particle:

$$\alpha_{p,j} = \sum_{n=0}^{N_p} \phi\left(r_{j,n}\right) V_{p,n} \tag{10}$$

where $\alpha_{p,j}$ is the volumetric concentration of particles (or particle fraction) in cell j [–], N_p is the number of particles contributing to the volumetric concentration in cell j [–], $V_{p,n}$ is the volume of particle n [m^3], j is the cell number, n is the particle number, $\phi(r_{j,n})$ is the kernel for mapping the particle information to the Eulerian mesh [m^{-3}], $r_{j,n}$ is the distance from the current cell centre j to the centre of particle n [m].

The same method is used for computing the interaction force per unit volume:

$$\boldsymbol{f}_j = \sum_{n=0}^{N_p} \phi\left(r_{j,n}\right) \boldsymbol{F}_{i,n} \tag{11}$$

where $\boldsymbol{f}_j$ is the interaction force between the fluid and discrete partcles acting on the fluid per unit volume for cell j [N/m^3] $\boldsymbol{F}_{i,n}$ is the interaction force between the fluid and the discrete particle n [N] which is equal to the negative value of the right hand side of Eq. (4).

In this study the Gaussian kernel is used as smoothing kernel:

$$\phi\left(r_{j,n}\right) = \frac{1}{\left(\sigma\sqrt{2\,\pi}\right)^{n_d}} \exp\left(-\frac{r_{j,n}^2}{2\,\sigma^2}\right) \quad \text{with} \quad r_{j,n} = \left\|\boldsymbol{c}_j - \boldsymbol{c}_{p,n}\right\| \tag{12}$$

where n_d is the number of spatial dimensions of the simulation [–], σ is the standard deviation of the Gaussian kernel [m], $\boldsymbol{c}_j$ is the location of the cell centre of cell j [m], $\boldsymbol{c}_{p,n}$ is the centre of particle n [m].

Xiao and Sun (2011) used the solution of the heat equation as a smoothing kernel. This solution of the heat equation can be obtained by multiplying the standard deviation in the Gaussian kernel with $\sqrt{2}$.

Evaluating every kernel function over all the cells in the domain is not efficient, since the contribution further away from the particle is negligible. Evaluating the kernel until 3 standard deviations includes 99% of the (theoretical) volume only leading to a minor error.

Sun and Xiao (2015b,a) relate the standard deviation to the particle diameter. In this study, the standard deviation is described as:

$$\sigma = \gamma\, d_p \tag{13}$$

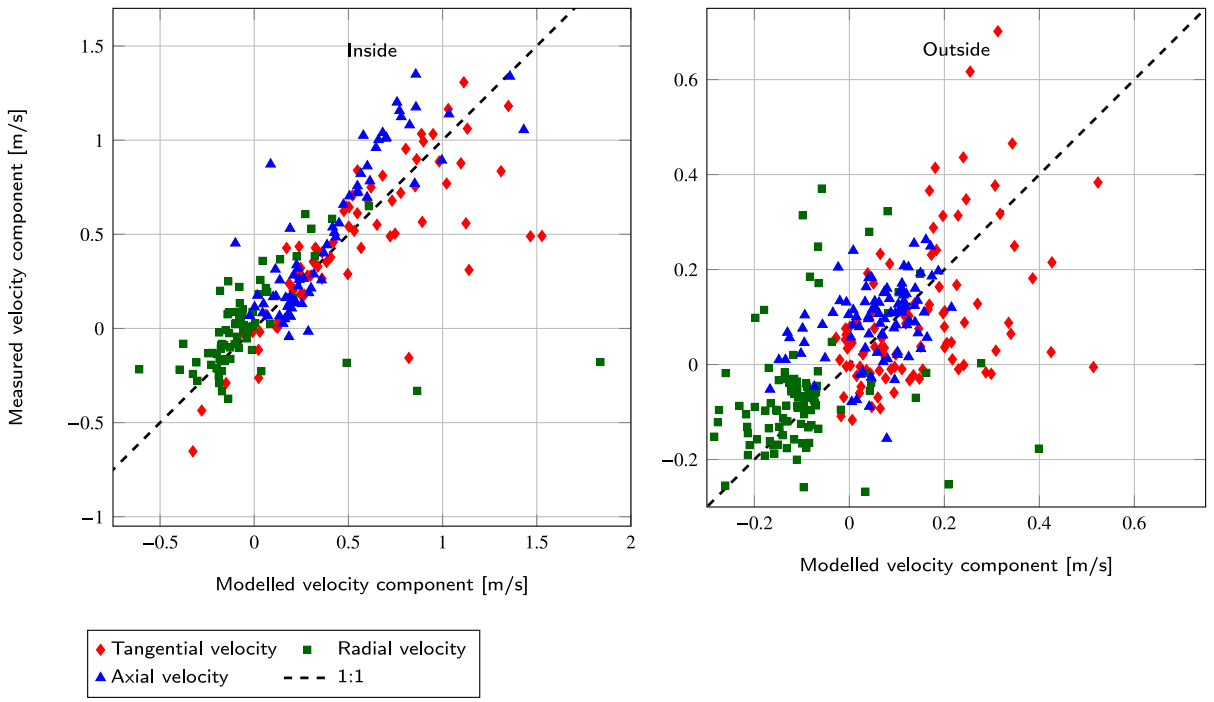

Fig. 5. Modelled velocities against the measured velocities for the 3 velocity components measured at the 12 location inside the cutter head and the 16 locations outside the cutter head.

where γ is the distance factor [–], leading to a radius of the influence sphere around the particle of: $3\,\gamma\,d_p$.

Fluid to particle

To compute the undisturbed fluid velocity at the particle for computing the drag force, the velocity at the Eulerian mesh needs to be mapped to the particles. For computing the added mass and the pressure gradient force, the total derivative of the fluid velocity also needs to be mapped. Lastly, the fluid fraction needs to be mapped to the particles for computing the concentration effect (Eq. (7)). Cells closer to the particle centre are more influenced by the particle, therefore a mapping is used which gives higher weights to velocities further away from the particle, ensuring less influence of the particle itself. For this purpose a quadratic function is used.

The quadratic distribution should have integral of unity over the domain $0 < r \leq R$ with $R = 3\,\sigma$. The integral of the weight factors is:

$$M = \int_V r^2 \,\mathrm{d}V \quad \text{with} \quad \mathrm{d}V = \left(r^2 \,\sin\theta\right) \mathrm{d}r\,\mathrm{d}\theta\,\mathrm{d}\varphi$$
$$M = \frac{4}{5}\,\pi\,R^5 \tag{14}$$

where M is integral of the weight factor ($r_{j,n}^2$) in the spherical domain [m^5], V is the volume of the spherical domain in the integration [m^3], R is the radius of the spherical domain [m], r, θ, φ are the radial coordinate, azimuthal angle and the polar angle, respectively.

Dividing the weight factor by its integral over the spherical domain, leads to the kernel function:

$$\psi(r_{j,n}) = \begin{cases} \frac{r_{j,n}^2}{M} = \frac{5}{4\,\pi\,R^5}\,r_{j,n}^2 & \text{for} \quad (r_{j,n}/3\,\sigma) < 1.0 \\ 0 & \text{for} \quad (r_{j,n}/3\,\sigma) \geq 1.0 \end{cases} \tag{15}$$

where $\psi(r_{j,n})$ is the kernel for mapping the Eulerian information to the particle [m^{-3}].

The fluid velocity and fluid fraction at the particle can be computed as:

$$\boldsymbol{u_{c|p,n}} = \sum_{j=0}^{N_{cells}} \psi\left(r_{j,n}\right)\, V_{cell,j}\, \boldsymbol{u_{c,j}} \tag{16}$$

$$\alpha_{c|p,n} = \sum_{j=0}^{N_{cells}} \psi\left(r_{j,n}\right)\, V_{cell,j}\, \alpha_{c,j} \tag{17}$$

where $\boldsymbol{u_{c|p,n}}$ is the undisturbed fluid velocity for particle n [m/s], $\boldsymbol{u_{c,j}}$ is the fluid velocity at cell j [m/s], N_{cells} is the number of cells in the spherical influence volume around a particle [–], $\psi(r_{j,n})$ is the kernel for mapping the Eulerian information of cell j to the particle n [m^{-3}], $\alpha_{c|p,n}$ is the fluid fraction at particle n [–], $\alpha_{c,j}$ is the fluid fraction at cell j [–].

Note that Eqs. (10) and (11) sum over the number of particles influencing a single cell, while Eqs. (16) and (17) sum over the cells in the influence volume of the particle.

Treatment of boundaries

The kernel functions needs to be scaled to ensure a correct treatment of the boundaries. Particles are mapped in a different manner at walls, processor interfaces and sliding mesh interfaces than in the middle of the domain. This section shows the scaling of the weight factors for mapping the particle properties to the fluid, while the mapping of fluid properties to the particles is performed in the same manner. In the case the kernel is not influenced by a boundary, the weight factors are divided by the sum of all the weight factors to ensure the sum equals to 1:

$$\phi_{tot,j} = \frac{\phi_{p,j}}{\sum_k^{N_{cells}} \phi_{p,k}} \tag{18}$$

where $\phi_{tot,j}$ is the scaled total kernel value for mapping the particle information to cell j [m^{-3}], $\phi_{p,k}$ is the non-scaled kernel value for mapping the information of cell k [m^{-3}].

For a correct representation of the particle fraction near a wall, a ghost particle is added at the other side of the wall at the same distance to the wall as the particle in the domain. This method is described in Xiao and Sun (2011) and leads to the following scaling of the weight factors:

$$\phi_{tot,j} = \frac{\phi_{p,j} + \phi_{gp,j}}{\sum_k^{N_{cells}} \phi_{p,k} + \sum_k^{N_{cells}} \phi_{gp,k}} \tag{19}$$

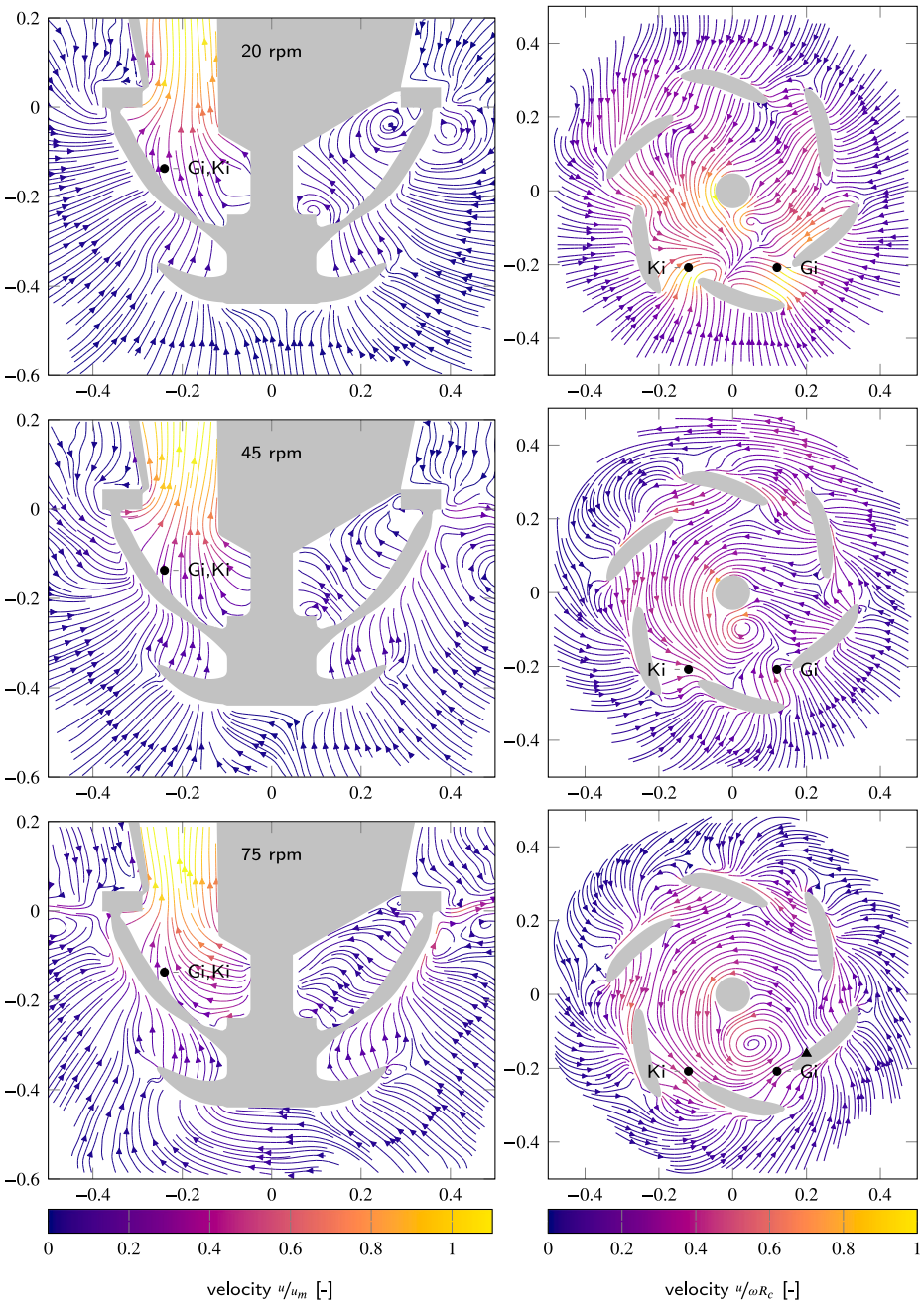

Fig. 6. Instantaneous streamlines for 3 different rotational velocities after 14 rotations. Top: 20 rpm, middle: 45 rpm and bottom: 75 rpm. The colours show the in-plane velocity magnitudes. The left plots show the yz-plane at x = 0. The right plots are cross-sections at 137 mm below the ring.

where $\phi_{gp,j}$, $\phi_{gp,k}$ are the non-scaled kernel value of the ghost particle at cell j and k [m^{-3}].

The particle properties such as velocity, position and size are exchanged between processors using openMPI. For the distributed particles, also the mapping functions need to be evaluated on both processors. The sum of the mapping function is transferred over the interface between the two processors for scaling the mapping function at both sides of the interface:

$$\phi_{tot,j} = \frac{\phi_{p,j}}{\sum_k^{N_{cells,K}} \phi_{p,k}^{procK} + \sum_m^{N_{cells,M}} \phi_{gp,m}^{procM}} \tag{20}$$

where $\phi_{p,k}^{procK}$ is the non-scaled kernel value at cell k on processor K [m^{-3}] and $\phi_{gp,m}^{procM}$ is the non-scaled kernel value of the ghost particle at cell m on processor M [m^{-3}].

At the sliding mesh interface the kernel functions do not extend to the other side. This has two reasons. The main reason is that OpenFOAM has the limitation that the sliding mesh should reside on a single processor for DEM simulations. Which means that the particle concentration should be spread across multiple interfaces: the processor interface and the sliding mesh interface. This leads to a complicated procedure. The second reason that it is more complicated to obtain the information of the cell at the other side of the sliding mesh is that the position of the connecting face between two neighboring cells changes over time.

This implementation leads to a discontinuity in time for the fluid phase when a particle passes a sliding mesh interface. In this case the time derivative of the concentration field will be high. As a result the simulation becomes unstable, due to the large return flow when the

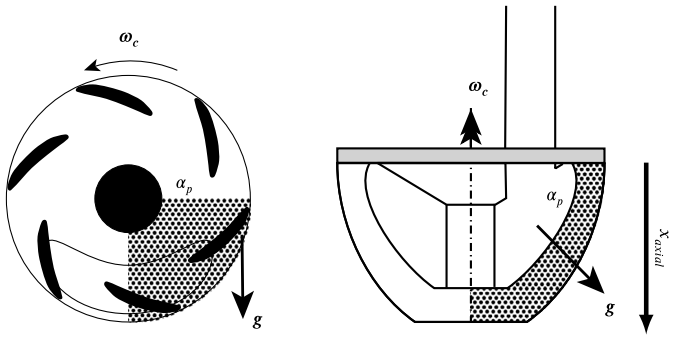

Fig. 7. Initial condition of the particle concentration (α_p) in the cutter head and the direction of the gravity acting on the particles.

particle crosses the sliding mesh interface. To solve this issue, the concentration change around the sliding mesh is not taken into account in the continuity equation. This causes an error in the continuity equation. However, in a test study with a settling particle it was observed that this error has the same magnitude as a standard computation without the usage of any mask functions. Unfortunately, the local error at the sliding interface is orders of magnitude larger compared to simulations with a stationary mesh.

Verification of method

The method is verified for a single, settling particle crossing the sliding mesh interface and for the settling of a cloud of particles in a two dimensional domain (using adapted kernel functions) for volumetric particle fractions of 0.02 up to 0.3. The simulation results are compared against a numerical integration of Eq. (4) using a zero undisturbed fluid velocity and an uniform particle fraction along the domain. For the single particle crossing the sliding mesh this resulted in a root mean square error of 0.01 m/s on a terminal settling velocity of 0.74 m/s.

2.4. Collisions

Inter-particle collisions and particles–wall collisions are computed using the method described by Tsuji et al. (1992), where the contact forces are computed by a so-called soft-sphere approach. This method uses a spring to model the rebound velocity and a viscous damper to model the energy dissipation during the collision. It is an extension of the collision model of Cundall and Strack (1979), which used a linear relation between the overlap distance and the collisional force. Tsuji et al. (1992) used a Hertzian (non-linear) spring for the relation between the force and displacement based on the work of Mindlin (1949) and Mindlin and Deresiewicz (1953). This method is already available in OpenFOAM and this paper extends the OpenFOAM spring–damper system with a formulation for computing the damping value to match measured coefficient of restitution. The normal and tangential force on a particle during a collision is computed as:

$$\boldsymbol{F_n} = -k_n \delta_n^{\frac{3}{2}} \boldsymbol{e_n} - \eta \, \boldsymbol{u_n} \tag{21}$$

$$\boldsymbol{F_t} = \begin{cases} -k_t \sqrt{\delta_n} \boldsymbol{\delta_t} - \eta \, \boldsymbol{u_t} & \text{for} \quad \|\boldsymbol{F_t}\| \leq \mu_f \, \|\boldsymbol{F_n}\| \\ -\boldsymbol{e_t} \, \mu_f \, \|\boldsymbol{F_n}\| & \text{for} \quad \|\boldsymbol{F_t}\| > \mu_f \, \|\boldsymbol{F_n}\| \end{cases} \tag{22}$$

$$\boldsymbol{\delta_t} = \sum_{t=0}^{t=t_{col}} \boldsymbol{u_t}^t \, \Delta t_{col} \tag{23}$$

where $\boldsymbol{F_n}$ and $\boldsymbol{F_t}$ are the normal and tangential collisional force component on the particle [N], k_n and k_t are the normal and tangential spring coefficient [N/m], $\boldsymbol{u_n}$ and $\boldsymbol{u_t}$ are the normal and tangential velocity of the particle [m/s], $\boldsymbol{u_t}^t$ is the tangential velocity of the particle at the contact point, thus including rotation at time t [m/s], η is the damping coefficient [N s/m], δ_n is the normal overlap distance [m], $\boldsymbol{\delta_t}$ is the tangential overlap vector [m], t_{col} and Δt_{col} are the collision time and the time step for the computing the collision [s], μ_f is the friction coefficient [–], $\boldsymbol{e_n}$ and $\boldsymbol{e_t}$ are the normal and tangential overlap unit vectors [–].

The spring coefficients are related to the combined properties of the particles (or particle and wall):

$$k_n = \frac{4}{3} \sqrt{R^*} \, E^* \qquad k_t = 8.0 \sqrt{R^*} \, G^* \tag{24}$$

where R^* is the effective radius [m], E^* is the effective modulus of Elasticity (Young's modulus) [N/m^2], G^* is the effective shear modulus [N/m^2].

For two particles with different properties (or a particle and a wall), the effective properties for the collision are:

$$\begin{aligned} \frac{1}{R^*} &= \frac{1}{R_i} + \frac{1}{R_j} \\ \frac{1}{M^*} &= \frac{1}{m_i} + \frac{1}{m_j} \\ \frac{1}{E^*} &= \frac{1 - \nu_i^2}{E_i} + \frac{1 - \nu_j^2}{E_j} \\ \frac{1}{G^*} &= \frac{2 - \nu_i}{G_i} + \frac{2 - \nu_j}{G_j} \end{aligned} \tag{25}$$

where R_i and R_j ate the radii of the two particles [m], M^* is the effective mass of the masses of the individual particles: m_i and m_j [kg], E_i and E_j are the moduli of elasticity of the two particles [N/m^2], G_i and G_j are the shear moduli of the two particles, ν_i and ν_j are the Poisson's ratio of both particles [–].

The relation between the modulus of elasticity and the shear modulus is:

$$E = 2\,G\,(1 + \nu) \tag{26}$$

The damping coefficient in Eqs. (21) and (22) is computed as:

$$\eta = \alpha_\eta \sqrt{M^* \, k_n} \, \delta_n^{\frac{1}{4}} \tag{27}$$

where α_η is an additional parameter [–].

This follows the assumption described by Tsuji et al. (1992) of an equal normal and tangential damping coefficient.

In the standard release of OpenFOAM, α_η is an input value. However, this is not a measurable parameter. Therefore this coefficient is linked to the particle Stokes number via the coefficient of restitution, which is a similar approach as used in Liggghts (Kloss, 2016). Antypov and Elliott (2011) showed an analytical relation between the damping coefficient and coefficient of restitution:

$$\alpha_\eta = -\sqrt{5} \, \frac{\ln \epsilon_n}{\sqrt{\ln^2 \epsilon_n + \pi^2}} \tag{28}$$

$$\epsilon_n = \frac{u_{n,in}}{u_{n,out}} \tag{29}$$

where ϵ_n is the coefficient of restitution in normal direction [–], $u_{n,in}$ is the magnitude of the normal incidence velocity before a collision [m/s], $u_{n,out}$ is the magnitude of the normal rebound velocity after a collision [m/s].

Legendre et al. (2006) showed a relation between the Stokes number and the coefficient of restitution:

$$\epsilon_{wet} = \epsilon_{dry} \, \exp\left(-\beta / \mathrm{St}_{AM}\right) \tag{30}$$

$$\mathrm{St}_{AM} = \frac{\left(\rho_s / \rho_f + C_{AM}\right) \, u_{n,in} \, d_p}{9\,\nu} \tag{31}$$

where ϵ_{wet} is the coefficient of restitution for wet (viscous) collisions [–], ϵ_{dry} is the coefficient of restitution for dry collisions [–], β is a empirical coefficient; a value of 35 was proposed by Legendre et al. (2006) [–], St_{AM} is the Stokes number, including the added mass of the fluid [–], ν is the kinematic viscosity of the fluid [m^2/s^2].

Table 1
Simulation parameters for the fluid simulation of a rotating cutter head.

Parameter	Quantity
Fluid	Water at 20 °C
Kinematic viscosity	$1.0034 \cdot 10^{-6}$ [m^2/s^2]
Domain	
Diameter	5 m
Height	1.31 m
Δx	4 mm
Operating condition	
Discharge Q_m	0.120 m^3/s
rot. velocity n_c	20, 30, 45, 60, 75, 90 rpm
Time step	
Co_{max}	0.9

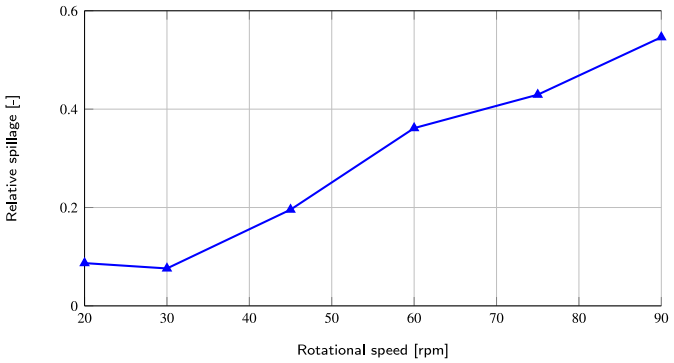

Fig. 8. Simulation result of relative spillage against rotational speed.

Using Eqs. (27), (28), (30) and (31) the viscous damping is related to the Stokes number.

In the simulations the shear modulus and corresponding Young's modulus of DEM-particles is reduced in order to match the particle collision time to the fluid simulation time step. Lommen et al. (2014) reduced the shear modulus and corresponding Young's modulus of DEM-particles by a factor 100. This showed limited influence on the penetration resistance of a wedge in soil. In this study, a reduction of the coefficient of restitution from 60 GPa to 10 Mpa yielded nearly no difference in rebound velocity and direction. These results showed a good agreement with the measured oblique particle–wall collisions by Joseph and Hunt (2004) and with the inter-particle collisions measured by Yang and Hunt (2006).

3. Results

The method described in the previous section will be used for simulating the flow in the rotating cutter and to model the flow induced spillage of a batch of particles.

3.1. Simulating flow

The fluid flow in the cutter head is validated for a 1 to 4 scale cutter head without any pickpoints. Nieuwboer et al. (2017) showed the validation of an even more simplified cutter head with an axi-symmetrical suction over the whole area of the back ring. Measurements of the flow velocities are published in Dekker et al. (2003). Fig. 3 shows a schematic drawing of the measurement setup including its dimensions. At 12 points inside the cutter head and 16 outside the cutter head velocities were measured using an Acoustic Doppler Velocimeter.

Simulation setup

The numerical domain for the simulation is a cylinder with a diameter of 5 m and a height of 1.31 m with the cutter head placed in the middle. This height is similar to the height of the water level in the experimental setup. The cutter is placed at the same distance from the bed as in the experiments, which is 0.39 m. This results in a 0.435 m clearance between the ring and the top of the domain. The mesh consists of $9.8 \cdot 10^5$ cells and has a minimum cell size of 4 mm at the blades, resulting in a $y^+_{avg} = 102$ for the 60 rpm simulation.

Table 1 shows more information on the domain and operating conditions. The suction discharge is not varied in these simulations and its value is 0.12 m^3/s. The rotational velocity is varied between 20 and 90 rpm.

All the walls in the simulation have a no slip boundary condition for the velocity. The inlet is located at the circumference of the cylinder and has a Dirichlet boundary for the velocity. The velocity boundary condition for the outflow at the top of the suction pipe is a Neumann boundary condition, imposing the discharge. All the pressure boundaries use the fixedFluxExtrapolatedPressure boundary condition, which sets the pressure gradient according to the predicted momentum, allowing possible non-zero pressure gradients at a rotating walls.

The advection term in the momentum equation is discretized using a using a blended scheme with 85%–90% central and 10%–15%upwind. Some areas with lower mesh quality initially caused the solution to become unstable. To overcome this issue, the blend factor was reduced to 60%–63% in the area underneath the ring. The simulation of the cutter head is first initialized using a steady state frozen rotor approach. Thereafter the simulation ran for 14 rotations of which the last 4 rotations are time-averaged to compare with the time-average results of the measurements.

Comparing simulation and measurements

Fig. 4 shows the measured and modelled velocity components at two points inside the cutter plotted against the rotational speed. The locations of these two points are indicated in Fig. 6. The measured velocities are shown by dotted lines with open markers and the simulation results are represented by solid lines with filled markers. The red lines shows the tangential velocities, defined positive in the rotational direction of the cutter head. Blue indicates the axial velocity, which is positive in the direction of the suction flow and the radial velocity, indicated in green, is positive for velocities flowing out of the cutter head.

At point Gi, the tangential velocity is dominated by the suction flow at low velocities leading to a negative (counter rotational) velocity. This effect is visible in both the measurements and the simulations and can be clearly seen in the streamlines in the right panes of Fig. 6. These streamlines are located in-plane with the measurement location Gi. The top pane shows the counter rotating flow at a low rotational speed and the two panes below show the streamlines for higher rotational speeds. At these two panes, the flow is co-rotating with the blades.

For the higher rotational speeds, the tangential velocity is not predicted well for point Gi. The right pane of Fig. 4 shows a sudden decrease in the measured tangential velocity at 75 rpm (the red dotted line), while the modelled value does not show this sudden decrease. The right panes of Fig. 6 can provide a possible explanation. It shows an eddy near the measurement location Gi. If the location of the eddy is not predicted correctly by the simulation or if the measurement location is slightly different than reported, this could lead to a large error in velocity at this point, since the velocity gradient is large in the eddy.

The tangential velocity at point Ki is only slightly under-predicted, while the trend of the measurements and the modelled velocities is similar. When the flow is a solid-body rotation, the tangential velocity would vary linearly with increasing rotational speed. The deviation at the lower rotational speeds is caused by the suction flow which forces a nearly counter-rotating flow (top right pane of Fig. 6).

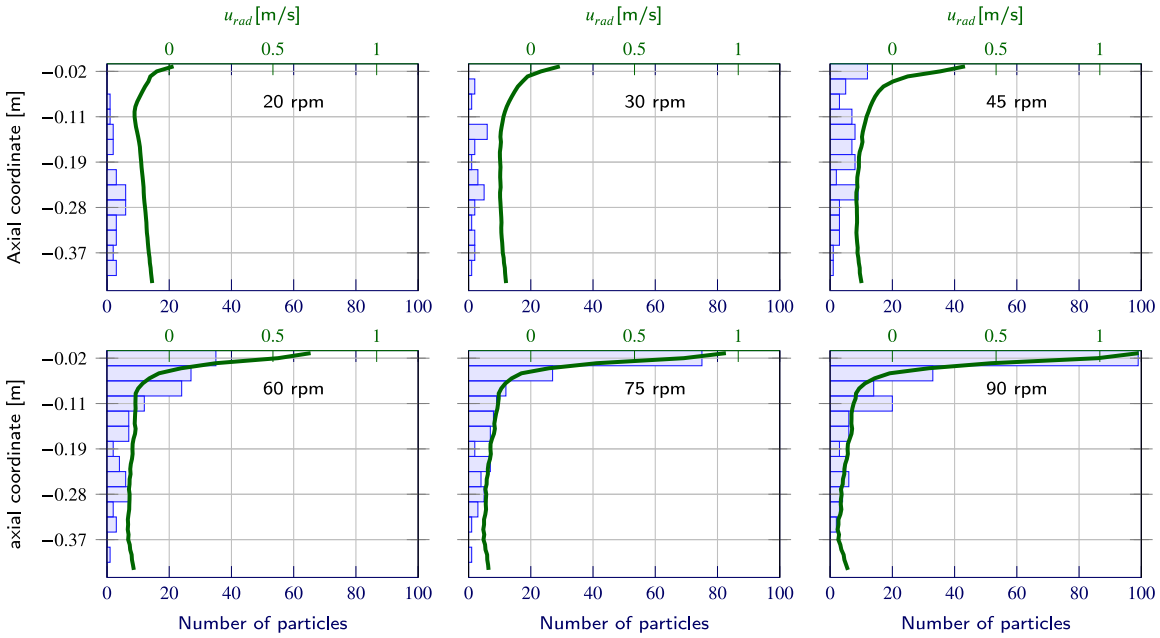

Fig. 9. Spillage and radial velocity over the axial coordinate. The bar plot shows the axial coordinate of spilled particles when they leave the contour of the cutter head. The 0 coordinate on the y-axis is at the ring and −0.44 is at the hub. The line plot shows the radial velocity averaged over both time and the azimuthal coordinate. The top axis corresponds to the radial velocities.

For both points, the radial velocity is predicted well. At point Ki, the increase in radial velocity from inflowing to out-flowing is visible in both the measurements and the simulation results, which can be more clearly seen in the streamline plots. At point Gi, the measurements show an increase in inflow for higher rotational velocity, while the simulations show a near constant value. This could also be attributed to the simulated position of the eddy. The measurements show nearly no tangential velocity, which is the case for a point at the east side of the eddy indicated by the triangle in the lower right pane of Fig. 6. At this point there is a radial in-flow and nearly no tangential velocity. This indicates that the location is of the eddy is not predicted correctly. For an increased rotational speed, the eddy will rotate faster increasing this radial velocity, which was visible in the measurements.

The axial velocity in both locations is under-estimated. This could be a numerical artefact, due to diffusion of momentum causing the flow being directed to the suction mouth over a larger area, resulting in a smaller axial velocity.

Fig. 5 shows the modelled against the measured values inside and outside the cutter head. The modelled velocities inside the cutter head correspond better to the measurements than the velocities outside the cutter head. The coarser mesh outside the cutter head is a possible explanation of this difference. Another explanation lies the measurement setup, since long waves in the basin were reported during the experiments. Also the return flow of the suction discharge into the basin could have had an effect on the velocity measurements.

Inside the cutter head, both radial and axial velocities are predicted quite well. The tangential velocities are over-predicted by the model which could be the effect of the location of the eddy. The rest of the velocity components lie closer to the 1:1 line.

3.2. Simulating flow induced spillage

The simulation of the flow induced spillage uses the same geometry and mesh as the simulation of the flow without particles.

Simulation setup

Similar to the simulation of the fluid flow in the cutter head, the flow for the spillage simulation is initialized using a steady state frozen rotor approach. Afterwards a single rotation is simulated using the unsteady method without any particles, leading to the initial situation for the spillage simulation. At the start of the spillage simulation, a single batch of particles is added between the blades to mimic the material entering the cutter head after it is cut. Fig. 7 indicates the volume where these particles placed with a dotted accent. This placement of the particles mimics the under-cut behaviour of the cutter head. The gravitational vector is pointing in an angle of 45 degrees from the rotational axis, resembling an inclination angle of 45 degrees. This is the same angle as Den Burger (2003) used, while a value of 25 to 30 degrees is more common in practice.

The simulation is a simplified representation of a working prototype cutter head. Only a single batch of particles is placed inside the cutter head, while in practice material flows continuously flows from the breach into the cutter head. In the simulation there is no breach present; this lack of confinement leads to an easier outflow of particles, increasing spillage. Also, the simulation does not model the hauling of the cutter head. The haul velocity could induce spillage since particles fall easier off a combined translating and rotating blade, than from a blade which only rotates.

Table 2 shows simulation settings for the spillage simulations. The domain and operating conditions are the same as for the fluid simulations (Table 1). To ensure a guaranteed stable simulation an upwind scheme is used for the advection of momentum. The distance factor (γ) of Eq. (13), determining the spreading of the concentration and force field, is taken 1.0.

Analysis of spillage and radial velocities

After a single rotation, nearly all the particles left the cutter for the 20 and 30 rpm case. For the higher rotational speeds, a fraction of 0.1 to 0.2 is left in the cutter, this is neither spilled nor transported.

Table 2
Simulation parameters for the flow induced spillage simulation.

Parameter	Quantity
Particle	
d_p	20 mm
ρ_p	2650 kg/m^3
E	10 Mpa
ν	0.24 (inter-particle) 0.27 (particle-steel)
μ_f	0.15
e_{dry}	0.97
dist. fac. γ	1.0
$N_{particles}$	368
d_{inter}	30 mm
c	0.155
Cutter head	
n_c	20, 30, 45, 60, 75, 90 rpm
Q_m	0.120 m^3/s
Fluid	
ρ_c	998.2 kg/m^3
ν	$1.0034 \cdot 10^{-6}$ m^2/s
Time step	
Co_{max}	0.5

The analysis disregards this fraction by assuming the same part of this fraction will be spilled as in the simulation.

Fig. 8 shows the flow induced spillage against the rotational speed and shows an increase in spillage with increasing rotational speed. Den Burger (2003) found the same trend in the measurements for higher rotational speeds and Zhang et al. (2018) found this trend is their simulations as well. However, the simulations do not show a decrease in spillage with increasing rotational speed as was observed in the experiments by Den Burger (2003). This could be caused by the absence of a breach, the method of feeding the particles and also the hauling velocity could play a role.

To check if the decrease in the production fraction is correlated to the out-flowing flux near the ring, Fig. 9 compares the radial velocities at the contour of the cutter head against the spillage over the axial coordinate of the cutter head. The horizontal bars show the height at which the particles flow out of the cutter head. For higher rotational speeds, more particles flow out of the cutter head. This is the most pronounced in the first 3 cm under the ring (the top bar in the figure). The line plot in the same figure shows the radial velocity at the hull-surface. This velocity is obtained from the simulations without particles (as described in Section 3.1) and it is time-averaged and averaged over the azimuthal coordinate. At the top bin under the ring, where most of the spillage occurs, the largest radial velocities are present.

Fig. 10 compares the relative spillage of the top bar to the outflow velocity at the same location. It shows the onset of spillage between a radial outflow velocity of 0.05 to 0.23 m/s. At higher velocities a non-linear relationship can be distinguished, however at the highest outflow velocity, the curve flattens. This non-linear relation could be caused by the drag being quadratically dependent on the radial velocity.

4. Conclusion

This paper shows a novel method for simulating flow induced spillage of rock particles in cutter heads. It can be used for designing a more energy efficient cutter head and working method of the Cutter Suction Dredger. Four methods are coupled to perform the spillage simulations: the Finite Volume Method for simulating the fluid flow, the Discrete Element Method for the motion of the rock particles, the soft-sphere collision model and lastly, the smoothing kernels for coupling of the Discrete Element Method with the Finite Volume Method in these simulations with large particle to mesh ratios.

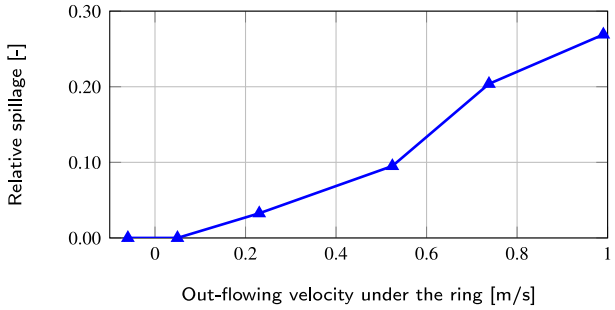

Fig. 10. The spillage part of the particles flowing out up to 3 cm under the ring against the outflow velocity at 1.5 cm under the ring. This is the spillage part of the top bars of Fig. 9 compared with the velocity in the middle of that bar.

These models are individually verified and validated for hindered settling, collisions and fluid flow in a rotating cutter head. The time-averaged fluid flow inside the cutter head compare well with the measurements of Dekker et al. (2003). However, the modelled velocities inside the cutter head compare better with the measurements than the velocities outside the cutter head.

In the simulations with particles, the results follow the same increase in spillage with increasing rotational speed as the measurements of Den Burger (2003) and the simulation results of Zhang et al. (2018). Additionally, these simulations show that the spillage occurs mostly just underneath the ring due to the combination of the centrifugal force and the shape of the blades.

5. Recommendations for future work

The presented simulations show the possibility to predict spillage of pieces of rock by using the DEM-FVM. The simulation uses a rotating cutter without a breach (cut-face) and only an initial amount of particles in the cutter. Further extension of the model towards modelling practical applications is possible by implementing a breach, a method to feed the cutter head with particles and simulating the translating motion. Implementing the breach around the cutter head will prevent particles from falling out. This can be implemented by making a boundary fitted mesh around the cutter head together with the breach or inserting a layer of particles. A continuous feed of particles is more realistic and will result in a better representation of spillage, since it ensures the simulation to predict a (dynamically) steady production.

Translating or hauling the cutter head will result in material falling off the blades, increasing the spillage at lower rotational velocities. The breach and the bed will prevent the particles falling out of reach of the blades of the cutter head.

This paper shows the amount of flow induced spillage. Analysis of particle trajectories and the forces on those particles can provide more details of the spillage process.

The sub-processes of spillage are validated and verified for this method. A next step would be to validate the spillage itself against for instance the measurements of Den Burger (2003). An even better validation would be to compare the simulated particle trajectories to measured trajectories.

List of symbols

A_p	Area of the particle projected to the flow direction [m^2]
$\boldsymbol{c_j}$	Location of the cell centre of cell j [m]
$\boldsymbol{c_{p,n}}$	Centre of particle n [m]
C_{AM}	Added mass coefficient, typically taken as 0.5 [–]
C_d	Drag coefficient [–]
d_p	Particle diameter [m]
$\boldsymbol{e_n}$	Normal overlap unit vectors [–]
$\boldsymbol{e_t}$	Tangential overlap unit vectors [–]
E_i, E_j	Moduli of elasticity of the two particles [N/m^2]
E^*	Effective modulus of Elasticity (Young's modulus) [N/m^2]
$\boldsymbol{f_i}$	Interaction force of the discrete particles acting on the fluid per unit volume [N/m^3]
$\boldsymbol{f_j}$	Interaction force between the fluid and discrete partcles acting on the fluid per unit volume for cell j [N/m^3]
$\boldsymbol{F_d}$	Drag force on a particle influenced by the concentration due to the presence of neighbouring particles [N]
$\boldsymbol{F_{d,0}}$	Drag force on a single particle in absence of surrounding particles [N]
$\boldsymbol{F_{i,n}}$	Interaction force between the fluid and the discrete particle n [N]
$\boldsymbol{F_n}$	Normal collision force component on the particle [N]
$\boldsymbol{F_t}$	Tangential collision force component on the particle [N]
$\boldsymbol{g}$	Gravitational acceleration [m/s^2]
G_i, G_j	Shear moduli of two colliding particles [N/m^2]
G^*	Effective shear modulus [N/m^2]
j	Cell number [–]
k	Cell number [–]
k_n	Normal spring coefficient [N/m]
k_t	Tangential spring coefficient [N/m]
m	Cell number [–]
m_i, m_j	Mass of the masses of two colliding particles [kg]
M	Integral of the weight factor (r^2) in the spherical domain [m^5]
M^*	Effective mass of the masses of the individual particles: m_i and m_j [kg]
n	Particle number [–]
n_c	Rotational speed of the cutter head [rpm]
n_d	Number of spatial dimensions of the simulation [–]
N_{cells}	Number of cells in the spherical influence volume around a particle [–]
N_p	Number of particles contributing to the volumetric concentration in cell j [–]
p	Pressure acting on the continuous phase [N/m^2]
Q_m	Mixture (or suction) discharge of the Cutter Suction Dredger [m^3/s]
r	Radial coordinate [m]
$r_{j,n}$	Distance from the current cell centre j to the centre of particle n [m]
R	Radius of the spherical domain [m]
R_i, R_j	Radii of the two particles [m]
R^*	Effective radius [m]
$\mathrm{Re_p}$	Reynolds number defined by the particle velocity [–]
$\mathrm{Re_s}$	Reynolds number defined by the slip velocity between the particles and the fluid [–]
St_{AM}	Stokes number, including the added mass of the fluid [–]
t	Time [s]
t_{col}	Collision time [s]
$\boldsymbol{u_c}$	Continuous phase (or fluid phase) velocity [m/s]
$\boldsymbol{u_{c,j}}$	Fluid velocity at cell j [m/s]
$\boldsymbol{u_{c\|p}}$	Undisturbed fluid velocity at the particle location [m/s]
$\boldsymbol{u_{c\|p,n}}$	Undisturbed fluid velocity for particle n [m/s]
$\boldsymbol{u_n}$	Normal velocity of the particle [m/s]
$u_{n,in}$	Magnitude of the normal incidence velocity of a particle before a collision [m/s]
$u_{n,out}$	Magnitude of the normal rebound velocity of a particle after a collision [m/s]
$\boldsymbol{u_p}$	Velocity of the particle [m/s]
$\boldsymbol{u_t}$	Tangential velocity of the particle [m/s]
$\boldsymbol{u_t}^t$	Tangential velocity of the particle at the contact point, thus including rotation at time t [m/s]
V_p	Volume of the particle [m^3]
$V_{p,n}$	Volume of particle n [m^3]
V	Volume of the spherical domain in the integration [m^3]
y^+_{avg}	Dimensionless wall distance averaged over the faces of the wall Defined by the wall distance, the shear velocity at the wall and the kinematic viscosity [–]
α_c	Continuous phase (or fluid phase) fraction [–]
$\alpha_{c,j}$	Fluid fraction at cell j [m/s]
$\alpha_{c\|p,n}$	Fluid fraction at particle n used for computing hindered settling [–]
α_p	Particle phase fraction [–]
$\alpha_{p,j}$	Volumetric concentration of particles (or particle fraction) in cell j [–]
α_η	Additional parameter for computing the damper in the spring–damper system [–]
β	Hindered settling exponent for the drag force [–]
β	Empirical coefficient in computing the coefficient of restitution. A value of 35 was proposed by Legendre et al. (2006) [–]
γ	Distance factor [–]
δ_n	Normal overlap distance [m]
$\boldsymbol{\delta_t}$	Tangential overlap vector [m]
Δx	Grid spacing [m]
Δt_{col}	Time step for the computing the collision [s]
ϵ_{dry}	Coefficient of restitution for dry collisions [–]
ϵ_n	Coefficient of restitution in normal direction [–]
ϵ_{wet}	Coefficient of restitution for wet (viscous) collisions [–]
η	Damping coefficient in the spring–damper system [N s/m]
θ	Azimuthal angle [rad]
μ_f	Friction coefficient [–]
ν	Kinematic viscosity [m^2/s^2]
ν_i, ν_j	Poisson's ratios of two colliding particles [–]
ρ_c	Continuous phase (or fluid phase) density [kg/m^3]
ρ_p	Density of the particle [kg/m^3]
σ	Standard deviation of the Gaussian kernel [m]
$\overline{\overline{\boldsymbol{\tau}}}$	Effective stress tensor including both the viscous and turbulent shear stresses acting on the fluid [N/m^2]
φ	Polar angle [rad]
$\phi_{gp,j}$	Non-scaled kernel value of the ghost particle at cell j [m^{-3}]
$\phi_{gp,k}$	Non-scaled kernel value of the ghost particle at cell k [m^{-3}]
$\phi^{procM}_{gp,m}$	Non-scaled kernel value of the ghost particle at cell m on processor M [m^{-3}]
$\phi_{p,k}$	Non-scaled kernel value for mapping the information of cell k [m^{-3}]
$\phi^{procK}_{p,k}$	Non-scaled kernel value at cell k on processor K [m^{-3}]
$\phi(r_{j,n})$	Kernel for mapping the particle information to the Eulerian mesh [m^{-3}]
$\phi_{tot,j}$	Scaled total kernel value for mapping the particle information to cell j [m^{-3}]
$\psi(r_{j,n})$	Kernel for mapping the Eulerian information of cell j to the particle n [m^{-3}]

CRediT authorship contribution statement

B.J. Nieuwboer: Writing – original draft, Conceptualization, Methodology, Software, Validation, Visualization. **C. van Rhee:** Writing – review & editing, Conceptualization, Supervision, Project administration, Funding acquisition. **G.H. Keetels:** Writing – review & editing, Methodology, Supervision.

Declaration of competing interest

The authors declare that they have no known competing financial interests or personal relationships that could have appeared to influence the work reported in this paper.

Data availability

Data will be made available on request.

Acknowledgements

The research presented in this paper has been funded by Royal Boskalis Westminster and Van Oord Dredging and Marine Contractors via Stichting Speurwerk Baggertechniek.

References

Antypov, D., Elliott, J.A., 2011. On an analytical solution for the damped Hertzian spring. Europhys. Lett. 94 (5), 50004.

Bigot, B., Bonometti, T., Lacaze, L., Thual, O., 2014. A simple immersed-boundary method for solid–fluid interaction in constant-and stratified-density flows. Comput. & Fluids 97, 126–142.

Brown, P.P., Lawler, D.F., 2003. Sphere drag and settling velocity revisited. J. Environ. Eng. 129 (3), 222–231.

Cundall, P.A., Strack, O.D.L., 1979. A discrete numerical model for granular assemblies. Geotechnique 29 (1), 47–65.

Dekker, M.A., Kruyt, N.P., Den Burger, M., Vlasblom, W.J., 2003. Experimental and numerical investigation of cutter head dredging flows. J. Waterw. Port Coast. Ocean Eng. 129 (October), 203–209, URL: http://ascelibrary.org/doi/abs/10.1061/(ASCE)0733-950X(2003)129:5(203).

Den Burger, M., 1997. Mixture forming in a cutterhead. In: Proceedings Ceda Dredging Days. Amsterdam, The Netherlands.

Den Burger, M., 2001. Mechanical transportation of particles induced by cutter blade geometry. In: Proceedings Ceda Dredging Days. Amsterdam, The Netherlands.

Den Burger, M., 2003. Mixture Forming Processes in Dredge Cutter Heads (Ph.D. thesis). Delft Universty of Technology.

Den Burger, M., Vlasblom, W.J., Talmon, A.M., 1999. Influence of operational parameters on dredge cutterhead spillage. In: Proceedings Ceda Dredging Days. Amsterdam, The Netherlands.

Den Burger, M., Vlasblom, W.J., Talmon, A.M., 2002. Particle trajectories along a cutter head blade, using the results of a CFD model for the flow. In: Proc. Dredging '02 Key Technologies for Global Prosperity, Orlando, USA. Amsterdam, The Netherlands.

Di Felice, R., 1994. The voidage function for fluid-particle interaction systems. Int. J. Multiph. Flow. 20 (1), 153–159.

Farrell, P.E., Maddison, J.R., 2011. Conservative interpolation between volume meshes by local Galerkin projection. Comput. Methods Appl. Mech. Engrg. 200 (1–4), 89–100. http://dx.doi.org/10.1016/j.cma.2010.07.015, URL: http://linkinghub.elsevier.com/retrieve/pii/S0045782510002276.

Hofman, J., 2015. Understanding DPMFoam/MPPICFoam. https://bugs.openfoam.org/file_download.php?file_id=1030&type=bug. [Online; accessed 21-05-2021].

Ishii, M., Hibiki, T., 2011. Thermo-Fluid Dynamics of Two-Phase Flow - Second Edition. Springer Science & Business Media.

Jasak, H., 1996. Error Analysis and Estimation for the Finite Volume Method with Applications to Fluid Flows (Ph.D. thesis). Imperial College, University of London.

Joseph, G.G., Hunt, M.L., 2004. Oblique particle–wall collisions in a liquid. J. Fluid Mech. 510, 71–93.

Kloss, C., 2016. LIGGGHTS(R)-public documentation, version 3.X. URL: https://www.cfdem.com/media/DEM/docu/Manual.html. [Online; accessed 22 September 2022].

Legendre, D., Zenit, R., Daniel, C., Guiraud, P., 2006. A note on the modelling of the bouncing of spherical drops or solid spheres on a wall in viscous fluid. Chem. Eng. Sci. 61 (11), 3543–3549.

Lommen, S., Schott, D., Lodewijks, G., 2014. DEM speedup: Stiffness effects on behavior of bulk material. Particuology 12, 107–112.

Manninen, M., Taivassalo, V., Kallio, S., 1996. On the Mixture Model for Multiphase Flow. Technical Report, VTT Energy.

Maxey, M.R., Riley, J.J., 1983. Equation of motion for a small rigid sphere in a nonuniform flow. Phys. Fluids 26 (4), 883–889.

Miedema, S.A., 2019. Dredging Engineering: Special Topics. TU Delft Open, http://dx.doi.org/10.5074/t.2019.004.

Mindlin, R.D., 1949. Compliance of elastic bodies in contact. J. Appl. Mech. 16 (3), 259–268. http://dx.doi.org/10.1115/1.4010702.

Mindlin, R.D., Deresiewicz, H., 1953. Elastic spheres in contact under varying oblique forces. J. Appl. Mech. 20 (3), 327–344. http://dx.doi.org/10.1115/1.4010702.

Nieuwboer, B.J., Keetels, G.H., Van Rhee, C., 2017. Flow Velocities in an Axi-Symmetrical Rotating Cutter Head. In: 18th International Conference on TRANSPORT and SEDIMENTATION of SOLID PARTICLES. Prague, Czech Republic, pp. 241–248.

Richardson, J.F., Zaki, W.N., 1954. The sedimentation of a suspension of uniform spheres under conditions of viscous flow. Chem. Eng. Sci. 3 (2), 65–73.

Royal Boskalis Westminster N.V., 2016. Boskalis: capabilities clip cutter suction dredger. URL: https://www.youtube.com/watch?v=PvwUitZewvw.

Shih, T.-H., Liou, W.W., Shabbir, A., Yang, Z., Zhu, J., 1995. A new k-ϵ eddy viscosity model for high reynolds number turbulent flows. Comput. & Fluids 24 (3), 227–238.

Slotta, L.S., 1968. Flow visualization techniques used in dredge cutter head evaluation. In: WODCON II. Rotterdam, The Netherlands, pp. 56–77.

Steinbusch, P.J., Vlasblom, W.J., Den Burger, M., Kruyt, N.P., 1999. Numerical simulation of the flow generated by cutter heads. In: Slurry Handling and Pipeline Transport, 14th International Conference, Hydrotransport 14. Maastricht, The Netherlands, pp. 435–443.

Sun, R., Xiao, H., 2015a. Diffusion-based coarse graining in hybrid continuum–discrete solvers: Applications in CFD–DEM. Int. J. Multiph. Flow. 72, 233–247.

Sun, R., Xiao, H., 2015b. Diffusion-based coarse graining in hybrid continuum–discrete solvers: Theoretical formulation and a priori tests. Int. J. Multiph. Flow. 77, 142–157.

Tsuji, Y., Tanaka, T., Ishida, T., 1992. Lagrangian numerical simulation of plug flow of cohesionless particles in a horizontal pipe. Powder Technol. 71 (3), 239–250.

Versteeg, H.K., Malalasekera, W., 2007. An Introduction to Computational Fluid Dynamics: The Finite Volume Method. Pearson Education.

Weller, H., 2005. Pressure-Velocity Solution Algorithms for Transient Flows. Technical Report. Technical Report TR/HGW/05, OpenCFD Ltd.

Werkhoven, J.J., Nieuwboer, B.J., Louis, A.A., Ramsdell, R.C., Miedema, S.A., 2018. A pseudo-analytical model CSD spillage due to rotational velocity-induced flow. In: Proceedings of the Western Dredging Association Dredging Summit & Expo'18. pp. 25–28.

Werkhoven, J., Nieuwboer, B., Ramsdell, R., Miedema, S., 2019. CSD spillage model for sand and rock. In: Proceedings of the 22nd World Dredging Congress. p. 17.

Xiao, H., Sun, J., 2011. Algorithms in a robust hybrid CFD-DEM solver for particle-laden flows. Commun. Comput. Phys. 9 (2), 297–323.

Yang, F.-L., Hunt, M.L., 2006. Dynamics of particle-particle collisions in a viscous liquid. Phys. Fluids 18 (12), 121506.

Zhang, M., Fan, S., Zhang, H., 2016. Flow field analysis of cutter head for cutter suction dredgers. In: International Conference on Human Centered Computing. Springer, pp. 578–587.

Zhang, M., Fan, S., Zhua, H., Han, S., 2018. Numerical simulation of solid-fluid 2-phase-flow of cutting system for cutter suction dredgers. Polish Marit. Res. 25 (s2), 117–124.

Zhou, Z., Kuang, S., Chu, K., Yu, A., 2010. Discrete particle simulation of particle-fluid flow: model formulations and their applicability. J. Fluid Mech. 661, 482.